PHYSICAL REVIEW C **95**, 064605 (2017)

Neutron scattering cross section measurements for ^{56}Fe

A. P. D. Ramirez,[1,*] J. R. Vanhoy,[2] S. F. Hicks,[3] M. T. McEllistrem,[1] E. E. Peters,[1] S. Mukhopadhyay,[1] T. D. Harrison,[2]
T. J. Howard,[3] D. T. Jackson,[3] P. D. Lenzen,[3] T. D. Nguyen,[3] R. L. Pecha,[3] B. G. Rice,[2] B. K. Thompson,[2] and S. W. Yates[1]
[1]*Departments of Chemistry and Physics & Astronomy, University of Kentucky, Lexington, Kentucky 40506, USA*
[2]*Department of Physics, U.S. Naval Academy, Annapolis, Maryland 21402, USA*
[3]*Department of Physics, University of Dallas, Irving, Texas 75062, USA*

(Received 25 January 2017; revised manuscript received 2 May 2017; published 9 June 2017)

Elastic and inelastic differential cross sections for neutron scattering from ^{56}Fe have been measured for several incident energies from 1.30 to 7.96 MeV at the University of Kentucky Accelerator Laboratory. Scattered neutrons were detected using a C_6D_6 liquid scintillation detector using pulse-shape discrimination and time-of-flight techniques. The deduced cross sections have been compared with previously reported data, predictions from evaluation databases ENDF, JENDL, and JEFF, and theoretical calculations performed using different optical model potentials using the TALYS and EMPIRE nuclear reaction codes. The coupled-channel calculations based on the vibrational and soft-rotor models are found to describe the experimental (n,n_0) and (n,n_1) cross sections well.

DOI: 10.1103/PhysRevC.95.064605

I. INTRODUCTION

Nuclear data play an important role in modeling future generation nuclear-energy systems [1–3]. Advanced high-temperature nuclear reactors, for example, are being designed for efficient energy generation while addressing safety, waste, and proliferation concerns. Several are under construction for use in the burn-up of heavy element radioisotopes associated with the large waste disposal pools from the operation of conventional energy-producing reactors. Computer models and simulations are used to predict the performance of these reactors under operating conditions, including the effects of severe irradiation on structural properties. These predictions require a vast knowledge of accurate and precise nuclear data, particularly cross sections from neutron-induced reactions.

Iron is one of the primary structural materials in many nuclear energy production systems, making Fe neutron scattering cross sections important input for neutron transport and energy absorption calculations. Elemental iron has four naturally occurring stable isotopes, with 91.75% abundant ^{56}Fe the most significant. In the fast-neutron energy region, the total cross sections for neutron-induced reactions on ^{56}Fe are dominated by elastic and inelastic scattering processes. A number of studies of fast-neutron scattering from ^{56}Fe have been reported [4–12]. Despite these efforts, there are still significant discrepancies among predictions from existing evaluated data libraries, particularly for the inelastic scattering processes [13]. Such discrepancies can be attributed to experimental data that have large or nonexistent uncertainties, lack of information on finite-size sample corrections, or inadequate inelastic scattering data [14]. In addition, sensitivity studies on important reactor quantities, such as criticality, require the reduction of neutron cross section uncertainties on actinides and structural materials to meet the target accuracies for advanced reactor designs [1–3]. Recent high-resolution measurements, performed using γ-ray spectroscopic techniques, have been published to provide data with reduced uncertainties [15–17].

In this paper, we present new experimental neutron elastic and inelastic scattering differential cross sections for ^{56}Fe. The experimental methods are discussed in Sec. II and analysis procedures in Sec. III. Our results and their comparisons to previously reported data, evaluation databases, and theoretical calculations obtained from well-established nuclear reaction codes are presented in Secs. IV and V.

II. EXPERIMENTAL METHODS

The ^{56}Fe fast-neutron scattering cross sections were measured at the University of Kentucky Accelerator Laboratory (UKAL). Monoenergetic bunched neutrons and time-of-flight (TOF) techniques were used to determine the scattered neutron energies. Neutrons were produced via the ^{3}H$(p,n)^3$He and the ^{2}H$(d,n)^3$He reactions for energies $E_n < 4.9$ and $E_n \geqslant 4.9$ MeV, respectively. In these reactions, the projectile protons or deuterons were accelerated using the UKAL 7-MV CN Van de Graaff accelerator. The terminal pulsing system, which features an rf-ion source, outputs pulsed beams at a repetition rate of 1.875 MHz and bunched to a width of about 1 ns with a klystron buncher.

The accelerated ions were then impinged upon a gas cell that contained the tritium or deuterium gas typically at 1-atm pressure. The 3-cm-long gas cell assembly consisted of a tantalum-lined stainless steel cylinder with a 3.3-μm-thick molybdenum entrance foil window. The energy spread of the emerging neutrons from the gas cell is dictated primarily by straggling of the incident ions in the entrance foil, energy losses of the ions in the gas, and sample size effects. For illustration, 6-MeV outgoing neutrons at 0° produced from ^{2}H$(d,n)^3$He reactions with 1 atm of deuterium gas have approximately a 170-keV energy spread, whereas 3-MeV neutrons produced from ^{3}H$(p,n)^3$He reactions have about an 80-keV energy spread.

---

[*] ap.ramirez@uky.edu

TABLE I. Geometries and masses of the scattering samples.

Sample	Height (cm)	Diameter (cm)	Mass (g)	Enrichment (%)
^{56}Fe	1.45	1.52	18.178	99.87
Polyethylene	1.49	0.96	1.069	

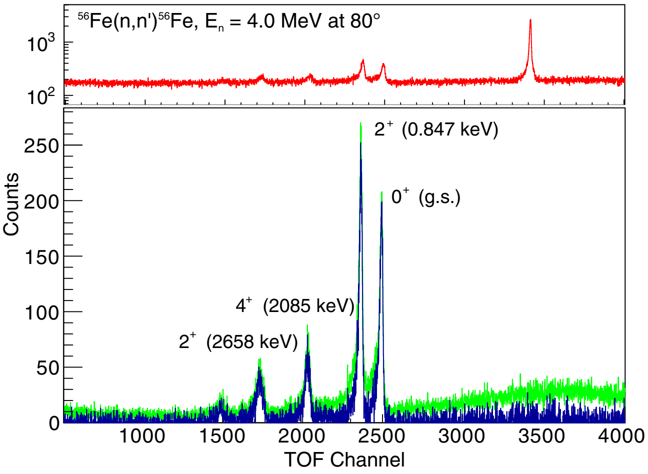

FIG. 1. Typical TOF spectra containing events from the detection of both neutrons and γ rays (red), neutrons only after pulse-shape discrimination (green), and also neutrons only after background subtraction (blue). In the top spectrum, peaks in the middle correspond to events from scattered neutrons while the largest peak on the right corresponds to events from the detection of prompt γ rays.

Scattered neutrons were registered using a neutron detector consisting of a C_6D_6 liquid scintillator coupled to a photomultiplier tube. The detector has pulse-shape discrimination (PSD) properties that allow the separation of neutron and unwanted γ-ray events. Furthermore, the TOF technique helps reduce time-uncorrelated neutron events.

To measure the angular distribution of scattered neutrons, the neutron detector was mounted on a goniometer that rotates through angles between 0° and 155° with respect to the beam direction. The pivot point was positioned at an axis set by the incident particle beam and (1) aligned to the center of the gas cell and (2) also aligned to the center of the scattering sample to measure the angular distribution of the source neutrons for the efficiency and cross section measurements, respectively. To minimize background from room-scattered neutrons, the neutron detector was surrounded by massive shields of lead and boron-loaded paraffin; additional massive shields of copper and paraffin were used as collimators. Moreover, a tungsten wedge was positioned near the gas cell to prevent the detector from a direct view of the neutron source for the angular distribution measurements. The goniometer can accommodate a flight path of up to 4 m.

An additional TOF detector, the forward monitor (FM), was set up to measure the neutrons emitted from the gas cell. The FM was positioned on the wall at an angle of 45° relative to the incident beam and was well collimated to view directly the gas cell. Due to the deep minimum in the neutron source cross sections at 45°, a second FM detector was set up at about 20° when using the ^{2}H(d,n)^{3}He reaction. The yield from the FM was used for relative normalization of the neutron fluence at the position of the scattering target.

The scattering samples used in these experiments were all right-circular cylinders in shape. The geometry and mass of each sample used are given in Table I. The polyethylene sample was used to obtain the absolute normalization for the measured cross sections through the H(n,n)H cross section standards found in the ENDF/B-VII.1 database [18,19]. For each emission angle, data were gathered for a "target in" (scattering sample suspended 7 cm away from the center of the gas cell) and for a "target out" (no target) measurement to account for the detected background neutrons. The final TOF spectra used for extracting the cross sections were obtained by subtracting the target-out from the target-in spectra (see Fig. 1).

The energy-dependent relative detector efficiencies were determined by comparing the neutron yields from the ^{3}H(p,n)^{3}He or the ^{2}H(d,n)^{3}He source reactions with their well-known cross sections [18–21]. Since the outgoing neutron energies vary as a function of scattering angle according to the kinematics of the source reaction, a wide neutron-energy range of the detector efficiency is obtained by measuring the angular distribution of the source neutrons. The detector efficiency at neutron energy E_n is determined using the equation

$$\varepsilon(E_n) = \frac{Y_{\mathrm{so}}(\theta_{\mathrm{lab}})}{Y_{\mathrm{FM}}\frac{d\sigma}{d\Omega_{\mathrm{lab}}}}, \tag{1}$$

where the Y_{so} is the neutron yield from the C_6D_6 detector at an emission angle θ_{lab}, Y_{FM} is the neutron yield from the forward monitor, and $\frac{d\sigma}{d\Omega_{\mathrm{lab}}}$ is the cross section of the source reaction at angle θ_{lab} retrieved from the DROSG-2000 program series [20,21]. An example of the C_6D_6 neutron detector efficiency is displayed in Fig. 2.

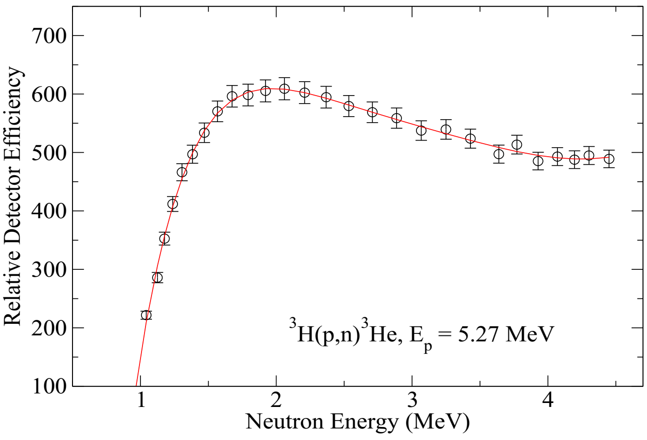

FIG. 2. Relative detector efficiency as measured from the angular distribution of the ^{3}H(p,n)^{3}He reaction and a sixth-order polynomial fit.

III. ANALYSIS

The neutron yields Y_{main} from the elastic and inelastic peaks in the TOF spectrum were extracted using the locally designed SAN12 fitting program that employed superimposed double Gaussian distributions with an exponential tail as the fitting function. Time-uncorrelated events in the spectrum were removed by using a linear fit to the background. The Y_{main} together with the forward monitor yield Y_{FM}, the detector efficiency $\varepsilon(E_n)$, the number of nuclei in the target N, and the absolute normalization factor A were used to determine the differential cross sections according to the formula

$$\frac{d\sigma}{d\Omega} = A\frac{Y_{\text{main}}}{\varepsilon(E_n)Y_{\text{FM}}N}. \tag{2}$$

The differential cross sections determined from Eq. (2) were corrected for neutron flux attenuation and multiple scattering in the sample using the well-established code MULCAT [22], a "forced collision" Monte Carlo program that follows only those neutrons whose trajectories from the scattering samples enter the solid angle subtended by the entrance to the detector shield. It neglects the scattering by air between the sample and detector, which greatly reduces the time required by a true Monte Carlo program. The code has been applied in previous studies mainly on isotopically enriched samples [23–27].

The Monte Carlo calculation requires the experimental elastic and inelastic differential cross sections in the laboratory frame, the neutron source differential cross sections, the total cross sections of the neutron reaction on the target nuclei, and the dimensions of the scattering sample and gas cell as input. The program outputs the corrected cross sections both in the laboratory and center-of-mass systems and the attenuation and multiple-scattering correction factors. Prior to using Eq. (2) for the $n + {}^{56}\text{Fe}$ scattering, it was initially applied to *n-p* scattering from the polyethylene sample to determine the absolute normalization factor A, using the procedures discussed in Ref. [23].

The estimated overall uncertainty for the present measurements is about 10%. The uncertainties in the MULCAT calculations for multiple scattering and finite-size corrections were estimated to be <5% [23]. This limit was inferred by comparing results between MULCAT and MCNP simulations [28]. The uncertainty in the detector efficiency was assumed to be 3% [23]. Uncertainties due to counting statistics were typically under 1–2%. The overall uncertainty is obtained by combining these contributions in quadrature.

IV. RESULTS

Neutron scattering differential cross sections were measured for selected incident neutron energies from 1.30 to 7.96 MeV covering the angles from 30° to 154°. The experimental cross sections presented throughout this paper are in the center-of-mass (c.m.) system with their overall absolute uncertainties.

These new experimental elastic scattering cross sections are compared with existing data from the literature [4,5,7–9,12] and evaluated data from ENDF/B-VII.1 [18], JEFF-3.1 [29], and JENDL-4.0 [30] compilations; these comparisons are shown in Fig. 3. Previously reported data [4–12] were retrieved from the experimental nuclear reaction data (EXFOR) database [31]. Reasonable agreement is observed among the evaluations and the experimental data for $E_n > 3.5$ MeV, while more variation is observed for $E_n \leqslant 3.5$ MeV. It should be noted that the total, elastic, and inelastic cross sections

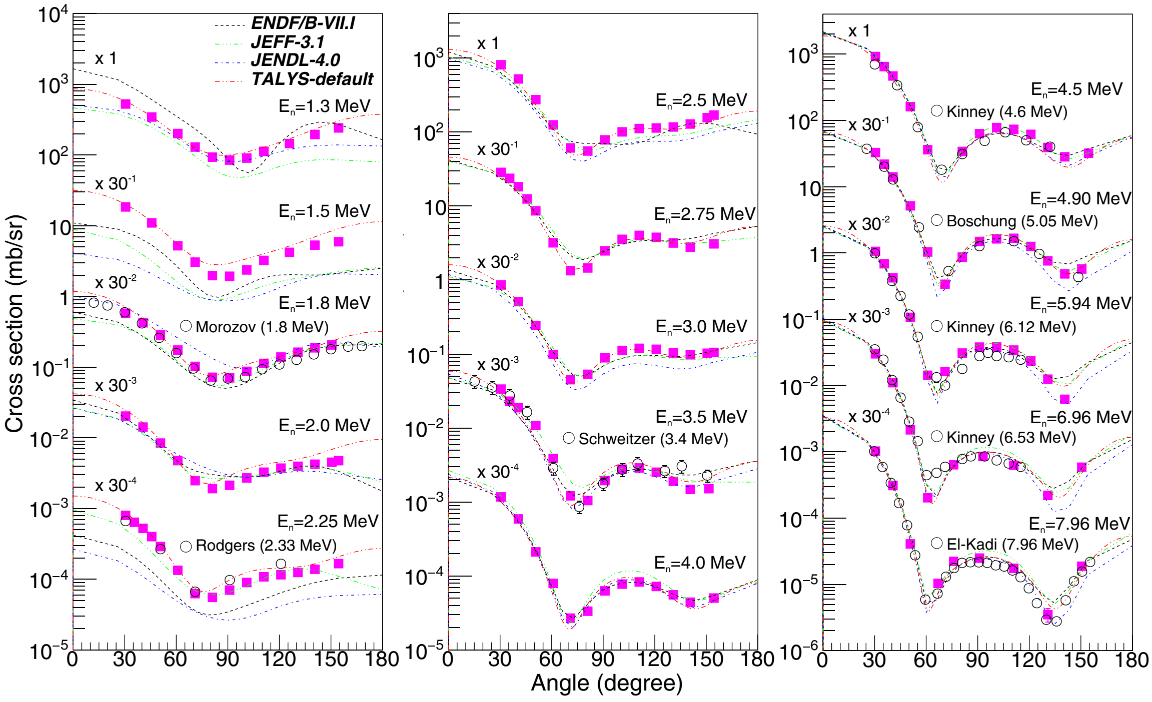

FIG. 3. The present experimental neutron elastic scattering differential cross sections for ^{56}Fe (solid points) compared with previously reported data [4,5,7–9,12] (open points), predictions from evaluation databases (curves, see key),, and theoretical calculations from TALYS.

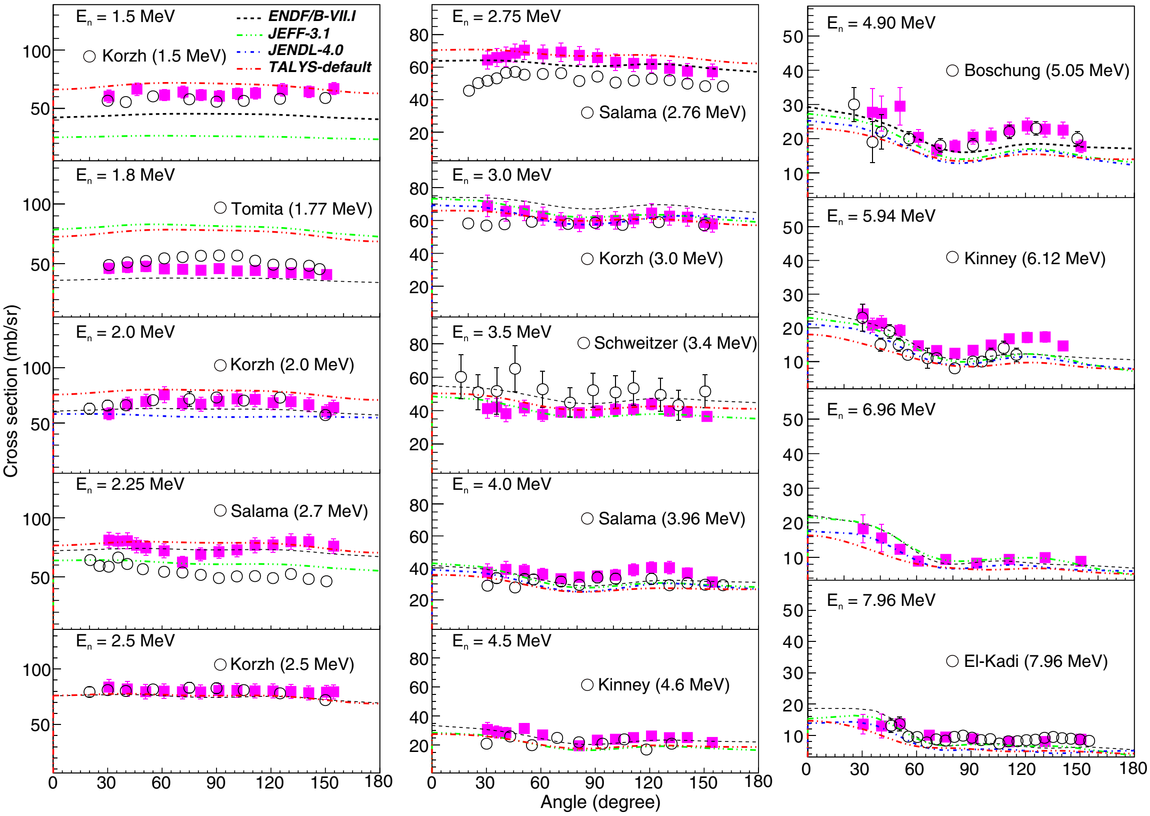

FIG. 4. The present experimental neutron differential cross sections for ^{56}Fe for the inelastic scattering populating the 847-keV level (solid points) compared with previously reported data [5–7,9–12] (open points), predictions from evaluation databases (curves, see key), and theoretical calculations from TALYS.

below 3.5 MeV rapidly fluctuate with energy due to narrow resonances. Our data, on the other hand, show the averaged cross sections over the incident neutron energy spread, which was larger than the average width of the fluctuations.

The angular distributions for the inelastically scattered neutrons populating the 2_1^+ excited state (n,n_1) of ^{56}Fe at 847 keV are shown in Fig. 4. The elastic and inelastic peaks are well resolved in the experimental data, but due to the large elastic cross sections at forward angles and the energy spread of the incident neutrons, the inelastic peak lies on the tail of the broad elastic peak. This overlap results in larger than average uncertainties for the (n,n_1) cross sections at angles below 50°. It is also noticeable in Fig. 4 that despite a difference of only tens of keVs, the previously reported cross sections for 2.25 and 2.75 MeV incident neutron energies from Ref. [11] are significantly lower than our values. Also, the angular distributions from incident energies above 4 MeV are found to be slightly forward peaked, and for $E_n \geqslant 4.9$ MeV this forward peaking becomes quite evident.

The (n,n_2) and (n,n_3) cross sections leading to the excitation of the 4_1^+ level at 2085 keV and the 2_2^+ level at 2657 keV in ^{56}Fe, respectively, were also obtained. The inelastic scattering from these levels demonstrates nearly isotropic angular distributions. Inelastic scattering from higher-lying levels was also observed, but was not investigated further because the states were unresolved experimentally.

In order to obtain the angle-integrated elastic and inelastic cross sections, we applied least-squares fits to our measured angular distributions using the Legendre polynomial expansion of the form

$$\frac{d\sigma}{d\Omega}(E_n,\theta_{\mathrm{c.m.}}) = \sum_{l=0}^{N} a_l(E_n)P_l(\cos\theta_{\mathrm{c.m.}}) \tag{3}$$

where P_l is a Legendre polynomial of order l and a_l is the expansion coefficient. For the elastic cross sections, the value of N is chosen such that the χ^2 is a minimum. The angle-integrated elastic cross sections for $E_n < 6.96$ MeV were found to vary within 5% when higher-order polynomials are included, while for neutron energies 6.96 and 7.96 MeV, the best fit was found only for $N = 7$. For the inelastic cross sections, the expansion was limited to $N = 2$ since the angular distributions are generally isotropic or only slightly forward peaked.

The angle-integrated neutron scattering cross sections (n,n_0), (n,n_1), and (n,n_2) are shown in Figs. 5(a)–5(c), respectively, as a function of incident neutron energy. The indicated uncertainties associated with the data points were obtained from the uncertainty of the $a_0(E_n)$ coefficient. For comparison, we included previously reported and evaluated data where the latter have been averaged over a 150-keV bin to lower the resolution and to remove the narrow fluctuations in the cross sections.

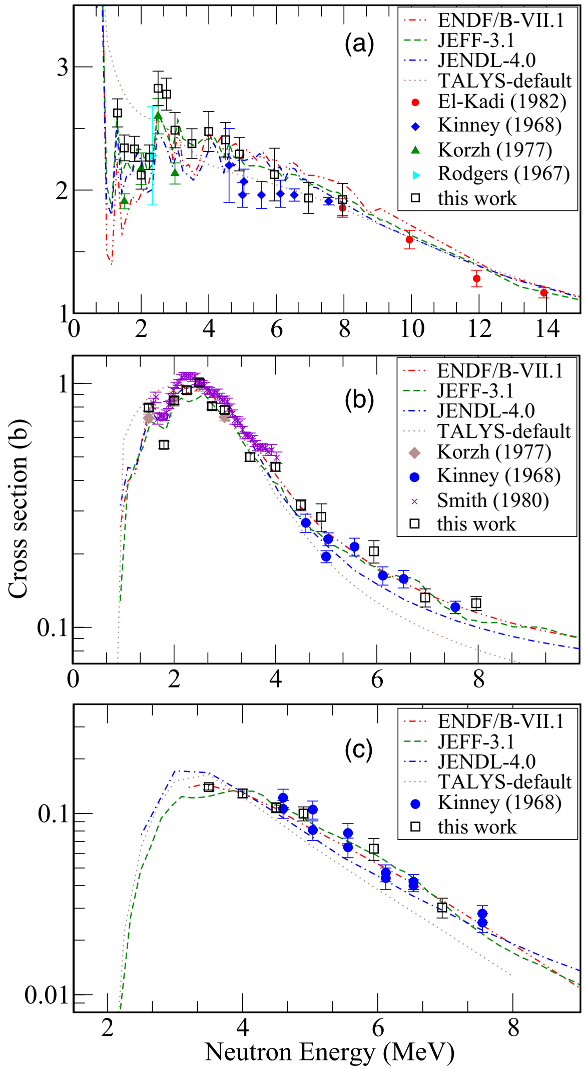

FIG. 5. Angle-integrated elastic (a) and inelastic scattering cross sections for excitation of the 847-keV (b) and 2085-keV (c) levels. Our experimental values (open points) are compared with existing data [4,5,10,12,32,33] (solid points) and evaluations and theoretical calculations (curves).

Our experimental neutron elastic scattering cross sections are fairly consistent with previously reported values in Refs. [4,5,10] and extrapolate well with values at higher neutron energies from Ref. [12]. The experimental data appear to follow closely the values from the JEFF database. For the (n,n_1) cross sections, our data are in good agreement with the evaluations and previously reported data in Refs. [4,5,10]. We have also compared our results with those obtained by Smith *et al.* in Refs. [32,33], which have extensive neutron scattering data on $^{\mathrm{nat}}$Fe in a similar bombarding energy range. As indicated in their paper [34], their inelastic scattering cross sections need to be corrected by 91.75% when compared with isotopic data. Their (n,n_1) angle-integrated cross sections are about 10% higher than our data, as shown in Fig 5(b).

Wenner *et al.* [35] carried out iron spherical shell measurements with neutrons using the $^2\mathrm{H}(d,n)^3\mathrm{He}$ reaction as the neutron source. They inferred from their results that neutron inelastic cross sections for ^{56}Fe at bombarding deuteron energies of $E_d = 3$, 5, and 7 MeV, corresponding to neutron energies of $E_n = 6.06$, 8.13, and 10.08 MeV, respectively, should be lower by at least 20% than those found in the evaluated data libraries. As our 5.94 and 7.96 MeV data are only slightly higher than the averaged ENDF values, the discrepancy that they observed in their measurements and simulations could not be attributed to the (n,n_1) cross section. It should be mentioned that although the (n,n_1) is a dominant inelastic scattering channel for $E_n = 6$ and 8 MeV, it only contributes about 12% and 8%, respectively, to the total inelastic cross section. Hence, complete knowledge of the inelastic scattering to higher-lying levels is required. Also, other nonelastic channels, such as the *(n,p)* process, contribute at these energies.

V. OPTICAL MODEL CALCULATIONS

We compared our experimental cross sections with theoretical values obtained from the nuclear reaction code TALYS [36]. The TALYS program is used to calculate cross sections using the conventional optical model and Hauser-Feshbach formalism [37,38] to account for direct and compound reaction mechanisms, respectively. A detailed description of the TALYS code can be found in Ref. [39].

The optical model is one of the primary foundations for nuclear observable calculations. For example, the solutions of the Schrödinger equation with the optical model potential, which fit data reasonably well, allow one to determine the cross sections from direct reaction mechanisms and transmission coefficients, which are necessary input to the Hauser-Feshbach or compound nucleus calculations. By default, TALYS uses the spherical optical model potential given by the expression

$$\begin{aligned}U(r,E) = &-V(E)f(r,a_V,R_V) - iW_V(E)f(r,a_V,R_V)\\ &+4ia_SW_S(E)\frac{d}{dr}f(r,a_S,R_S)\\ &+V_{\mathrm{SO}}(E)\left(\frac{\hbar}{m_\pi c}\right)^2\frac{1}{r}\frac{d}{dr}f(r,R_{\mathrm{SO}},a_{\mathrm{SO}})(\mathbf{l}\cdot\sigma)\\ &+iW_{\mathrm{SO}}(E)\left(\frac{\hbar}{m_\pi c}\right)^2\frac{1}{r}\frac{d}{dr}f(r,R_{\mathrm{SO}},a_{\mathrm{SO}})(\mathbf{l}\cdot\sigma), \quad (4)\end{aligned}$$

where the parameters $V(E)$, $W_V(E)$, $W_S(E)$, $V_{\mathrm{SO}}(E)$, and $W_{\mathrm{SO}}(E)$ are the energy-dependent potential-well depths for the volume V, surface S, and spin-orbit (SO) components. The energy dependence of the aforementioned parameters can also be found in Ref. [36]. The form factor f follows a Woods-Saxon shape given by the equation

$$f(r_i,R_i,a_i) = \frac{1}{1+\exp\left[(r_i-R_i)/a_i\right]}, \quad (5)$$

where the a_i are the diffuseness parameters and the R_i are the radii defined by $R_i = r_iA^{1/3}$, with A as the mass number, for each term. For this work, we employed the optical model parameters based on the global Koning-Delaroche parametrization [40], which was derived from an extensive set of neutron and proton experimental data for spherical nuclei. The optical model parameters used in the calculations for $E_n = 6.96$ and 7.96 MeV are given in Table II.

TABLE II. Default spherical optical model potential parameters used in the TALYS calculations.

E (MeV)	V_V (MeV)	r_V (fm)	a_V (fm)	W_V (MeV)	W_D (MeV)	r_{V_D} (fm)	a_{V_D} (fm)	V_{SO} (MeV)	$r_{V_{\mathrm{SO}}}$ (fm)	$a_{V_{\mathrm{SO}}}$ (fm)	W_{SO} (MeV)
6.96	50.48	1.186	0.663	0.52	7.50	1.282	0.532	5.71	1.000	0.580	−0.03
7.96	50.11	1.186	0.663	0.59	7.61	1.282	0.532	5.69	1.000	0.580	−0.04

The experimental elastic scattering angular distributions are very well described by the theoretical values (see Fig. 3), although a slight overestimation by the calculations for $E_n \leqslant 2.5$ MeV is observed. This overestimation is also found in the angle-integrated cross sections shown in Fig 5(a). As mentioned earlier, the total, elastic, and (n,n_1) cross sections are dominated by resonance fluctuations which may not be properly taken into account by the energy-averaged optical model calculations. At angles larger than 60°, the compound elastic contribution is comparable in magnitude with the shape elastic ones. The compound process exhibits angular distributions that are symmetric about 90° in the c.m. system, hence their contribution in the forward angles is negligible. In the calculations, the compound cross sections have undergone width fluctuations corrections using the Moldauer formalism to account for the correlation between the incident and outgoing waves in the elastic scattering channel, which results in an enhancement of the elastic scattering cross section. As the bombarding energy increases, the compound cross sections continue to decrease rapidly due to the opening of other nonelastic channels. For energies above 6 MeV, the compound component is so negligible that the total elastic cross sections can be entirely attributed to the shape elastic contribution.

For the (n,n_1) cross sections, however, the theoretical values obtained using the default TALYS optical parameters are largely underestimated for bombarding energies above 3.5 MeV [see Figs. 4 and 5(b)]. When using the spherical optical potential in TALYS, the inelastic cross sections are calculated using the distorted wave Born approximation (DWBA) that assumes weak coupling between the elastic and the discrete low-lying excited levels. This method is inappropriate for collective nuclei, such as ^{56}Fe, which have been shown to demonstrate vibrational, rotational, or rotational-vibrational low-lying collective levels [41–43]. When calculating cross sections, such collective properties are taken into account using the coupled-channel formalism.

To better describe the inelastic scattering cross sections, TALYS was used to perform coupled-channel calculations to compare with our experimental data. The harmonic vibrational model was applied where the radii in the optical potential are expressed as

$$R_i = r_i A^{1/3}\left[1 + \sum_{\lambda\mu} \alpha_{\lambda\mu} Y_\lambda^\mu(\Omega)\right].$$

The $\alpha_{\lambda\mu}$ operators are related to the coupling strength β_λ. In this case, we assumed vibrational coupling between the first 0^+ and 2^+ states only via a quadrupole one-phonon exchange. The cross sections for populating the higher discrete low-lying levels are still calculated using the DWBA. The same optical potential parameters based on the global Koning-Delaroche parametrization with the imaginary surface potential depth W_D reduced by 64% from the default values were used in the calculation. Employing these parameters in the coupled-channel calculation preserves the spherical optical model fit to our elastic scattering data.

The results of the coupled-channel calculations based on the vibrational model are shown in Fig. 6. Better agreement with the experimental (n,n_1) cross sections from 6.96- and 7.96-MeV bombarding energies is observed. The coupling parameter β_2 for the first 2^+ state is assumed to be 0.24, which is the same as that in the compilation from Ref. [44].

There are existing local and global optical model potentials for coupled-channel calculations for neutrons incident on ^{56}Fe that have been suggested from earlier studies [41–43]. Soukhovitskii *et al.* [42] suggest the use of the soft-rotor coupled-channel optical model as an effective tool to predict neutron-induced reactions on nuclei using their known collective structure. The coupling strengths, which are enhanced compared to those from the rigid-rotor model, used in the coupled-channel calculation are derived from the wave functions of the soft-rotor model Hamiltonian. The Hamiltonian parameters are optimized to provide the rotational-vibrational energy spectra for the low-lying collective levels of the nucleus of interest.

The experimental data were compared with predictions from dispersive coupled-channel optical model calculations based on the soft-rotor model. In this framework, the real and imaginary parts of the potential are related by a dispersion

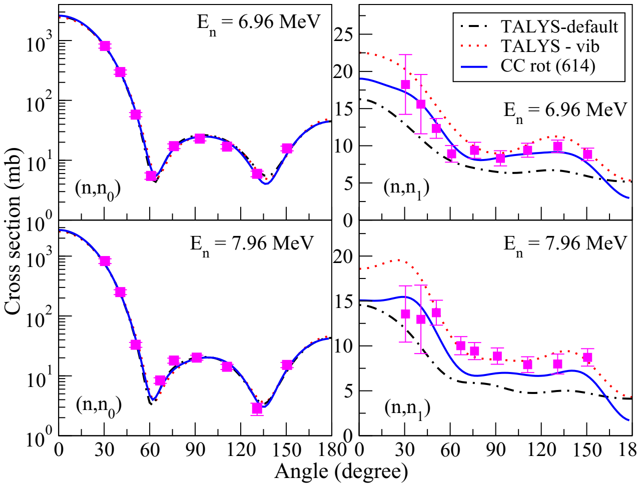

FIG. 6. Comparison between the present experimental cross sections (points) and coupled-channels calculations using TALYS with the default (dashed-dotted) and adjusted (dotted) parameters, and RIPL-3 parameter systematics obtained from Ref. [42] (solid).

TABLE III. Experimental and calculated angle-integrated cross sections based on spherical (sph), vibrational (vib), and soft-rotor (soft-rot) models for elastic, (n,n_1), (n,n_2), and (n,n_3) neutron scattering on ^{56}Fe. Cross sections are in units of b.

E_n (MeV)	Channel	Expt. (this work)	TALYS (sph)	TALYS (vib)	CC-rot (soft-rot)
4.00	(n,n_0)	2.48(17)	2.21	2.18	2.06
	(n,n_1)	0.455(20)	0.348	0.411	0.413
	(n,n_2)	0.129(8)	0.123	0.123	0.159
	(n,n_3)	0.175(8)	0.154	0.152	0.179
4.50	(n,n_0)	2.41(15)	2.160	2.14	2.098
	(n,n_1)	0.317(17)	0.254	0.311	0.306
	(n,n_2)	0.108(8)	0.091	0.092	0.116
	(n,n_3)	0.125(8)	0.115	0.115	0.131
4.90	(n,n_0)	2.29(15)	2.12	2.10	2.11
	(n,n_1)	0.284(37)	0.199	0.254	0.238
	(n,n_2)	0.100(9)	0.071	0.071	0.083
5.94	(n,n_0)	2.13(21)	2.05	2.03	2.07
	(n,n_1)	0.205(22)	0.129	0.182	0.157
	(n,n_2)	0.064(9)	0.039	0.038	0.047
6.96	(n,n_0)	1.94(13)	1.96	1.94	1.99
	(n,n_1)	0.132(11)	0.098	0.151	0.125
	(n,n_2)	0.030(5)	0.023	0.022	0.031
7.96	(n,n_0)	1.92(13)	1.85	1.83	1.87
	(n,n_1)	0.126(10)	0.081	0.134	0.105

relation reducing significantly the number of optical potential parameters [45]. Here, we adopted the parameters from Ref. [43], which can be retrieved from the reference input parameters library (RIPL-3) [46] with index number 614. The parameters from Ref. [43] are assumed to be valid for iron isotopes with mass numbers between 54 and 58 and incident neutron energies between 1 keV and 250 MeV. These parameters were used as input to the nuclear reaction program EMPIRE [45] to calculate neutron elastic and inelastic cross sections. The calculations include the code OPTMAN [47] which incorporates level-coupling schemes based on a non-axial soft-rotor model to account for the stretching of soft nuclei by rotations.

The comparison between our data and the dispersive coupled-channel calculation based on the soft-rotor model from Ref. [43] at $E_n = 6.96$ and 7.96 MeV are shown in Fig. 6. A tabulation of the calculated cross sections from different model calculations is given in Table III. Only the data for $E_n \geqslant 4$ MeV are presented since these cross sections are shown to vary smoothly with bombarding energy according to the ENDF evaluations. All the models were able to describe the elastic cross sections well within 10% for $E_n \geqslant 4.90$ MeV. The (n,n_1) cross sections obtained from the coupled-channel formalism using the optical potential parameters from Ref. [43] better describe the data than the spherical optical model calculations, although a noticeable underestimation is found for neutron energies 4.90 and 5.94 MeV. For the (n,n_2) and (n,n_3) cross sections, most of the theoretical values are found to be smaller than the experimental ones. The (n,n_2) and (n,n_3) cross sections from TALYS vibrational and spherical model calculations are almost identical as both are calculated using the DWBA.

VI. CONCLUSION

The angular distributions for neutron scattering from ^{56}Fe were measured at 15 incident neutron energies from 1.30 to 7.96 MeV. The neutron scattering cross sections deduced from these data have been compared with values from evaluation databases. Reasonable agreement has been observed for data above 3.5 MeV, although our data tend to be closer to the cross sections from the JEFF library. Our angle-integrated (n,n_1) cross sections, representing the dominant inelastic channel for neutron energies of 5.94 and 7.96 MeV, are slightly higher than those in the evaluations. This result does not support the assertion of Wenner *et al.* [35] that the total inelastic cross section from the ENDF database should be lower by at least 20%.

We have also compared our experimental results with predictions from theoretical calculations using TALYS with default parameters and coupled-channel calculations based on the vibrational model, as well as the EMPIRE nuclear reaction code based on the soft-rotor model with optical model potential parameters from Ref. [43]. In general, the calculations were able to describe the present differential elastic scattering cross sections well, particularly for neutron energies above 4.5 MeV. When the TALYS default were used to calculate the (n,n_1) cross sections through the DWBA method, the predictions significantly underestimated the experimental data for $E_n > 3.5$ MeV. The TALYS predictions can be improved by employing the coupled-channel vibrational model but with a 64% reduction in the imaginary surface potential depth. Similarly, the EMPIRE calculations based on the soft-rotor model were also found to describe the inelastic cross sections well.

ACKNOWLEDGMENTS

The authors acknowledge the many contributions of H. E. Baber to these measurements. This research was funded in part by the U.S. DOE NNSA-SSAA under Grant No. DE-NA0002931, U.S. DOE NEUP under Grant No. NU-12-KY-UK-0201-05, U.S. NSF under Grant No. PHY-1305801, and the Donald A. Cowan Physics Institute at UD.

---

[1] G. Palmiotti and M. Salvatores, J. Nucl. Sci. Technol., **48**, 612 (2011).

[2] G. Rimpault, in *Proceedings of the International Workshop on Nuclear Data Needs for Generation IV Nuclear Energy Systems, Belgium, 2005*, edited by P. Rullhusen (World Scientific, Singapore, 2006), pp. 18–31.

[3] G. Aliberti, G. Palmiotti, M. Salvatores, T. K. Kim, T. A. Taiwo, I. Kodeli, E. Sartori, J. C. Bosq, and J. Tommasi, in *Proceedings*

of the International Workshop on Nuclear Data Needs for Generation IV Nuclear Energy Systems, Belgium, 2005, edited by P. Rullhusen (World Scientific, Singapore, 2006), pp. 81–100.
[4] W. L. Rodgers, E. F. Shrader, and J. T. Lindow, Chicago Operations Office, A.E.C., Prog. Report COO-1573-33, p. 2 (1967).
[5] W. E. Kinney, Oak Ridge National Laboratory Report ORNL-TM-2052 (1968).
[6] Y. Tomita, K. Tsukada, M. Maruyama, S. Tanaka, in *Proceedings of the Second International Conference on Nuclear Data for Reactors*, Vol. II (IAEA, Helsinki, 1970), p. 301.
[7] P. Boschung, J. T. Lindow, and E. F. Shrader, Nucl. Phys. A **161**, 593 (1971).
[8] V. M. Morozov, Y. G. Zubov, and N. S. Lebedeva, Sov. J. Nucl. Phys. **17**, 381 (1973).
[9] Th. Schweitzer, D. Seeliger, and S. Unholzer, IAEA Reports IAEA-190-2, 243 (1976).
[10] I. A. Korzh, V. A. Mishchenko, E. N. Mozhzhukhin, N. M. Pravdivy, and I. E. Sanzhur, Ukr. Fiz. Zh. **22**, 87 (1977).
[11] M. Salama, Atomkernenergie **37**, 221 (1981).
[12] S. M. El-Kadi, C. E. Nelson, F. O. Purser, R. L. Walter, A. Beyerie, C. R. Gould, and L. W. Seagondollar, Nucl. Phys. A **390**, 509 (1982).
[13] M. B. Chadwick, E. Dupont, E. Bauge, A. Blokhin, O. Bouland, D. A. Brown, R. Capote, A. Carlson, Y. Danon, C. De Saint Jean, M. Dunn, U. Fischer, R. A. Forrest, S. C. Frankle, T. Fukahori, Z. Ge, S. M. Grimes, G. M. Hale, M. Herman, A. Ignatyuk, M. Ishikawa, N. Iwamoto, O. Iwamoto, M. Jandel, R. Jacqmin, T. Kawano, S. Kunieda, A. Kahler, B. Kiedrowski, I. Kodeli, A. J. Koning, L. Leal, Y. O. Lee, J. P. Lestone, C. Lubitz, M. MacInnes, D. McNabb, R. McKnight, M. Moxon, S. Mughabghab, G. Noguere, G. Palmiotti, A. Plompen, B. Pritychenko, V. Pronyaev, D. Rochman, P. Romain, D. Roubtsov, P. Schillebeeckx, M. Salvatores, S. Simakov, E. Soukhovitskii, J. C. Sublet, P. Talou, I. Thompson, A. Trkov, R. Vogt, and S. van der Marck, Nucl. Data Sheets **118**, 1 (2014).
[14] S. F. Hicks, J. R. Vanhoy, A. J. French, S. L. Henderson, T. J. Howard, R. L. Pecha, Z. C. Santonil, B. P. Crider, S. Liu, M. T. McEllistrem, E. E. Peters, F. M. Prados-Estevez, T. J. Ross, and S. W. Yates, EPJ Web Conf. **93**, 02002 (2015).
[15] R. O Nelson, N. Fotiades, M. Devlin, J. A. Becker, P. E. Garrett, and W. Younes, AIP Conf. Proc. **769**, 838 (2005).
[16] A. Negret, C. Borcea, Ph. Dessagne, M. Kerveno, A. Olacel, A. J. M. Plompen, and M. Stanoiu, Phys. Rev. C **90**, 034602 (2014).
[17] R. Beyer, R. Schwengner, R. Hannaske, A. R. Junghans, R. Massarczyk, M. Anders, D. Bemmerer, A. Ferrari, A. Hartmann, T. Kogler, M. Roder, K. Schmidt, and A. Wagner, Nucl. Phys. A **927**, 41 (2014).
[18] M. B. Chadwick, M. Herman, P. Oblozinsky, M. E. Dunn, Y. Danon, A. C. Kahler, D. L. Smith, B. Pritychenko, G. Arbanas, R. Arcilla, R. Brewer, D. A. Brown, R. Capote, A. D. Carlson, Y. S. Cho, H. Derrien, K. Guber, G. M. Hale, S. Hoblit, S. Holloway, T. D. Johnson, T. Kawano, B. C. Kiedrowski, H. Kim, S. Kunieda, N. M. Larson, L. Leal, J. P. Lestone, R. C. Little, E. A. McCutchan, R. E. MacFarlane, M. MacInnes, C. M. Mattoon, R. D. McKnight, S. F. Mughabghab, G. P. A. Nobre, G. Palmiotti, A. Palumbo, M. T. Pigni, V. G. Pronyaev, R. O. Sayer, A. A. Sonzogni, N. C. Summers, P. Talou, I. J. Thompson, A. Trkov, R. L. Vogt, S. C. van der Marck, A. Wallner, M. C. White, D. Wiarda, and P. G. Young, Nucl. Data Sheets **112**, 2887 (2011).
[19] A. Carlson, V. G. Pronyaev, D. L. Smith, N. M. Larson, Z. Chen, G. M. Hale, F. J. Hambsch, E. V. Gai, S. Y. Oh, S. A. Badikov, T. Kawano, H. M. Hofmann, H. Vonach, and S. Tagesen, Nucl. Data Sheets **110**, 3215 (2009).
[20] M. Drosg, IAEA Report IAEA-NDS-87, Rev. 9 (2005).
[21] H. Liskien and A. Paulsen, At. Data Nucl. Data Tables **11**, 569 (1973).
[22] J. R. Lilley, MULCAT-BRC, A Monte Carlo Neutron and Gamma-Ray Multiple Scattering Correction Program, Internal Service de Physique et Techniques Nucléaire, Centre d'Études de Bruyères-le-Châtel, Report P2N/934/80 (1980).
[23] J. R. Vanhoy, S. F. Hicks, A. Chakraborty, B. R. Champine, B. M. Combs, B. P. Crider, L. J. Kersting, A. Kumar, C. J. Lueck, S. H. Liu, P. J. McDonough, M. T. McEllistrem, E. E. Peters, F. M. Prados-Estevez, L. C. Sidwell, A. J. Sigillito, D. W. Watts, and S. W. Yates, Nucl. Phys. A **939**, 121 (2015).
[24] S. F. Hicks, J. M. Hanly, S. E. Hicks, G. R. Shen, and M. T. McEllistrem, Phys. Rev. C **49**, 103 (1994).
[25] S. F. Hicks, S. E. Hicks, G. R. Shen, and M. T. McEllistrem, Phys. Rev. C **41**, 2560 (1990).
[26] S. E. Hicks, Z. Cao, M. C. Mirzaa, J. L. Weil, J. M. Hanly, J. Sa, and M. T. McEllistrem, Phys. Rev. C **40**, 2509 (1989).
[27] M. C. Mirzaa, J. P. Delaroche, J. L. Weil, J. Hanly, M. T. McEllistrem, and S. W. Yates, Phys. Rev. C **32**, 1488 (1985).
[28] T. Goorley, M. James, T. Booth, F. Brown, J. Bull, L. J. Cox, J. Durkee, J. Elson, M. Fensin, R. A. Forster, J. Hendricks, H. G. Hughes, R. Johns, B. Kiedrowski, R. Martz, S. Mashnik, G. McKinney, D. Pelowitz, R. Prael, J. Sweezy, L. Waters, T. Wilcox, and T. Zukaitis, Los Alamos National Laboratory Report LA-UR-13-22934 (2013).
[29] OECD/NEA Data Bank, The JEFF-3.1.1 Nuclear Data Library, JEFF Report 22, OECD/NEA Data Bank (2009).
[30] K. Shibata, O. Iwamoto, T. Nakagawa, N. Iwamoto, A. Ichihara, S. Kunieda, S. Chiba, K. Furutaka, N. Otuka, T. Ohsawa, T. Murata, H. Matsunobu, A. Zukeran, S. Kamada, and J. Y. Katakura, J. Nucl. Sci. Technol. **48**, 1 (2011).
[31] N. Otuka, E. Dupont, V. Semkova, B. Pritychenko, A. I. Blokhin, M. Aikawa, S. Babykina, M. Bossant, G. Chen, S. Dunaeva, R. A. Forrest, T. Fukahori, N. Furutachi, S. Ganesan, Z. Ge, O. O. Gritzay, M. Herman, S. Hlavac, K. Kato, B. Lalremruata, Y. O. Lee, A. Makinaga, K. Matsumoto, M. Mikhaylyukova, G. Pikulina, V. G. Pronyaev, A. Saxena, O. Schwerer, S. P. Simakov, N. Soppera, R. Suzuki, S. Takacs, X. Tao, S. Taova, F. Tarkanyi, V. V. Varlamov, J. Wang, S. C. Yang, V. Zerkin, and Y. Zhuang, Nucl. Data Sheets **120**, 272 (2014).
[32] D. L. Smith, Argonne National Laboratory Report ANL/NDM-20 (1976).
[33] A. B. Smith and P. T. Guenther, Nucl. Sci. Eng. **73**, 186 (1980).
[34] A. B. Smith, Nucl. Phys. A **605**, 269 (1996).
[35] M. T. Wenner, A. Haghighat, J. M. Adams, A. D. Carlson, S. M. Grimes, and T. N. Massey, Nucl. Sci. Eng. **170**, 207 (2012).
[36] A. J. Koning, S. Hilaire, and M. C. Duijvestijn, in *Proceedings of the International Conference on Nuclear Data for Science and Technology, France, 2007*, edited by O. Bersillon, F. Gunsing, E. Bauge, R. Jacqmin, and S. Leray, EDP Sciences (2008), pp. 211–214.
[37] W. Hauser and H. Feshbach, Phys. Rev. **87**, 366 (1952).
[38] L. Wolfenstein, Phys. Rev. **82**, 690 (1951).
[39] TALYS 1.6 manual, http://www.talys.eu
[40] A. J. Koning and J. P. Delaroche, Nucl. Phys. A **713**, 231 (2003).

[41] J. P. Delaroche,, S. M. El-Kadi, P. P. Guss, C. E. Floyd, and R. L. Walter, Nucl. Phys. A **390**, 541 (1982).

[42] E. Sh. Soukhovitskii, S. Chiba, J. Y. Lee, B. T. Kim, and S. W. Hong, J. Nucl. Sci. Technol. **40**, 69 (2003).

[43] R. Li, W. Sun, E. Sh. Soukhovitskii, J. M. Quesada, and R. Capote, Phys. Rev. C **87**, 054611 (2013).

[44] S. Raman, C. W. Nestor, and P. Tikkanen, At. Data Nucl. Data Tables **78**, 1 (2001).

[45] M. Herman, R. Capote, B. V. Carlson, P. Oblozinsky, M. Sin, A. Trkov, H. Wienke, and V. Zerkin, Nucl. Data Sheets **108**, 2655 (2007).

[46] R. Capote, M. Herman, P. Oblozinsky, P. G. Young, S. Goriely, T. Belgya, A. V. Ignatyuk, A. J. Koning, S. Hilaire, V. A. Plujko, M. Avrigeanu, O. Bersillon, M. B. Chadwick, T. Fukahori, Z. Ge, Y. Han, S. Kailas, J. Kopecky, V. M. Maslov, G. Reffo, M. Sin, E. Sh. Soukhovitskii, and P. Talou, Nucl. Data Sheets **110**, 3107 (2009).

[47] E. Soukhovitski, S. Chiba, O. Iwamoto, K. Shibata, T. Fukahori, and G. B. Morogovskij, Programes OPTMAN and SHEMMAN, Version 8 (2004), Japan Atomic Energy Research Institute, Rep. JEARI-Data/Code-2005-002 (2005).